Supporting Information

Sing et al. 10.1073/pnas.0906489107

SI Text

Computer Simulations. Our system consists of N superparamagnetic beads of radius a, which interact through a potential U. The dynamics of each bead can be modeled by using the Langevin equation:

$$\frac{\partial}{\partial t}\mathbf{r_i} = \sum_{j}^{N}(\mu_{\mathbf{ij}} \cdot \nabla_{\mathbf{r_j}} U(t) + \nabla_{\mathbf{r}_j} \cdot \mathbf{D}_{ij}) + \xi_i(t), \qquad [S1]$$

where $\mu_{\mathbf{ij}}$ is the mobility matrix, $\mathbf{D}_{ij}$ is the diffusion tensor defined as $\mathbf{D}_{ij} = k_B T \mu_{ij}$, and $\xi_i(t)$ is a random force that satisfies $\langle \xi_i(t)\xi_j(t')\rangle = 2k_b T \mu_{\mathbf{ij}}\delta(t-t')$. In our simulations, $\mu_{\mathbf{ij}}$ accounts for the hydrodynamic interactions between the beads and is given by a generalization of the Blake tensor (1, 2) that incorporates the finite size of the beads. One can simply say it corresponds to a Rotne–Prager–Blake tensor (3–5). For the present article we do not include the random noise term $\xi_i(t)$ because the magnetic forces dominate the dynamics, as is shown below, and in accordance with the experimental results.

The conserved force on the beads, $F = -\nabla_{\mathbf{r_j}} U(t)$, is given by four contributions: the excluded volume interactions between two beads F_b, the boundary repulsion between the wall and beads F_w, the gravitational force F_g, and the magnetic dipole-dipole force F_B that is induced when the field is applied. The excluded volume potential is simply

$$U_b(r) = \begin{cases} \infty & r \le 2a, \\ 0 & r > 2a, \end{cases} \qquad [S2]$$

where a is the radius of a particle and r is the distance between the beads. For computational convenience, this potential is approximated by a modified Lennard–Jones potential that has a corresponding force given by

$$F_b(r) = \frac{\epsilon}{r-2a}\left[\left(\frac{\sigma}{r-2a}\right)^{12} - \left(\frac{\sigma}{r-2a}\right)^{6}\right] \qquad [S3]$$

with $\sigma = 0.1a$. The strength of the force is governed by ϵ that was chosen to be $0.02k_bT$ to render the attraction term negligible. The repulsive force between the wall and the beads, which acts only on the z direction, is given by a similar potential:

$$U_w(r_z) = \begin{cases} \infty & r_z \le a, \\ 0 & r_z > a, \end{cases} \qquad [S4]$$

where r_z is the distance from the wall to the center of the beads. This potential is also approximated by a modified Lennard–Jones potential, with a corresponding force of the form

$$F_w(z) = \frac{\epsilon}{r_z-a}\left[\left(\frac{\sigma}{r_z-a}\right)^{12} - \left(\frac{\sigma}{r_z-a}\right)^{6}\right]. \qquad [S5]$$

All other parameters are the same as above.

The applied magnetic field on the superparamagnetic particle induces a magnetic dipole moment on each of the beads. Because the field is relatively small, we are in the linear regime and thus can assume that the magnetic moment $\mathbf{m}$ is both in the direction of and proportional to the applied field. Also, the induction time is much smaller than the typical rotation time of the aggregate, so that the process is taken to be instantaneous. The moment is calculated by using the relationship

$$\mathbf{m} = \frac{V_c \Delta\chi}{\mu_0}\mathbf{B}, \qquad [S6]$$

where μ_0 is the magnetic permittivity, $V_c = 4\pi a^3 f/3 = 0.42\ \mu m^3$ is the effective volume of the paramagnetic bead ($f = 0.1$ is the fraction of the actual bead that is paramagnetic and $a = 1\ \mu m$ is the bead radius), and $\Delta\chi = 0.7$ is the magnetic susceptibility difference between the bead and the medium (water). The values given here are those used in the simulation and correspond to the values quoted by Invitrogen for their superparamagnetic beads. There is both a component of B due to the applied magnetic field and the dipole moments of the surrounding beads (separated by a distance r), which is neglected in our simulations. Because the magnetic field creates a moment in the direction of the applied field, the force due to the induced dipole, F_B, is given by the dipole-dipole force (6, 7):

$$F_B^{ij} = \frac{3\mu_0}{4\pi r^4}\left(\left(\frac{\mathbf{m_i}\cdot\mathbf{r_{ij}}}{r}\right)\mathbf{m_j} + \left(\frac{\mathbf{m_j}\cdot\mathbf{r_{ij}}}{r}\right)\mathbf{m_i}\right) - \left(\left(\frac{5(\mathbf{m_j}\cdot\mathbf{r_{ij}})(\mathbf{m_i}\cdot\mathbf{r_{ij}})}{r^2} - (\mathbf{m_i}\cdot\mathbf{m_j})\right)\frac{\mathbf{r_{ij}}}{r}\right), \qquad [S7]$$

where r is the distance between the center of the beads, $\mathbf{r_{ij}}$ is the position vector between beads i and j, and $\mathbf{m_i}$ and $\mathbf{m_j}$ are the magnetic moments of beads i and j, respectively. By considering a characteristic magnetic moment $m_0 = \frac{V_c\Delta\chi}{\mu_0}B_0$ and defining a characteristic length scale equivalent to the radius of the bead a, we can rewrite this equation in terms of dimensionless distances $\tilde{\mathbf{r}} = \mathbf{r}/a$ and dimensionless moments $\tilde{\mathbf{m}} = \mathbf{m}/m_0$:

$$\tilde{F}_B^{ij} = \frac{F_0}{\tilde{r}^4}\left(\left(\frac{\tilde{\mathbf{m}_i}\cdot\tilde{\mathbf{r}_{ij}}}{\tilde{r}}\right)\tilde{\mathbf{m}_j} + \left(\frac{\tilde{\mathbf{m}_j}\cdot\tilde{\mathbf{r}_{ij}}}{\tilde{r}}\right)\tilde{\mathbf{m}_i}\right) - \left(\left(\frac{5(\tilde{\mathbf{m}_j}\cdot\tilde{\mathbf{r}_{ij}})(\tilde{\mathbf{m}_i}\cdot\tilde{\mathbf{r}_{ij}})}{\tilde{r}^2} - (\tilde{\mathbf{m}_i}\cdot\tilde{\mathbf{m}_j})\right)\frac{\tilde{\mathbf{r}_{ij}}}{\tilde{r}}\right), \qquad [S8]$$

where the magnitude of the magnetic force can be characterized by a single parameter $F_0 = \frac{4\pi}{3\mu_0}(af\Delta\chi B)^2$, which comes from the substitution of Eq. **4** into Eq. **5**. For the experimental conditions, one finds $F_0 \sim 100k_bT/a$, which implies that the fluctuation term is negligible, as mentioned before.

Finally, the gravitational force due (at the Earth's surface) is simply $F_g(z) = -\Delta\rho V g$, where we have used the gravitational acceleration $g = 9.8\ m/s^2$, the difference between the bead and water densities $\Delta\rho = 0.8\ g/cm^3$, and the bead volume $V = 4\pi a^3/3$.

The final form of the Langevin equation for a given bead is written in dimensionless form with $\tilde{r} = r/a$ and $\tilde{t} = t/\tau$, where $\tau = a^2/(\mu_0 k_B T)$ is the characteristic diffusion time:

$$\tilde{\mathbf{r}}_\mathbf{i}(\tilde{t}+\Delta\tilde{t}) = \tilde{\mathbf{r}}_\mathbf{i}(\tilde{t}) + \Delta\tilde{t}(\tilde{\mu}_\mathbf{ij}\cdot(\tilde{\mathbf{F}}_\mathbf{j,b} + \tilde{\mathbf{F}}_\mathbf{j,w} + \tilde{\mathbf{F}}_\mathbf{j,B} + \tilde{\mathbf{F}}_\mathbf{j,g})). \qquad [S9]$$

For a given set of conditions, the simulation is run with a time step $\Delta\tilde{t} = 0.001$ for 1×10^7 iterations (or more than 10 full rotations of the magnetic field).

Experimental Setup. The magnetic field is created by using a pair of Helmholtz coils, each with 300 windings at a radius of 45 mm (see Fig. S1). To induce a rotating magnetic field we use a $\pi/2$ phase-shifted sinusoidal signal for each coil. The signal was amplified by a low frequency amplifier to gain an electric current of adequate

strength to achieve a maximum magnetic field of 10 mT. The frequency could be varied between 5 and 1000 Hz.

The sample is enclosed by the Helmholtz coils and is mounted on an inverted fluorescent microscope equipped with phase contrast (Zeiss, Axiovert 200M). The microscope can be tilted by 90°, and therefore samples can be observed from the side (as in Fig. 1*B*).

Magnetic beads were purchased by Invitrogen (Dynabeads MyOne Carboxylic Acid) in aqueous solution.

The phospholipid vesicles were prepared by electroswelling (8). In all experiments we used the lipid 1,2-Dioleoyl-sn-Glycero-3-Phosphocholine (DOPC, Avanti Polar Lipids) without further purification. We added a small amount (0.1% wt/wt) of the fluorescently labeled lipid, Texas red 1,2-dihexadecanoyl-sn-glycero-3-phosphoethanolamine (Texas red DHPE, Invitrogen) to the DOPC lipid. The vesicles were swollen in a 200 mM sucrose solution and injected into an isoosmotic glucose filled chamber for the experiments. Because of the slightly higher density of sucrose, the vesicles settle down on the bottom of the sample chamber.

Walking Velocity of a Single Rotor. We can analytically solve for the walking velocity of a single rotor by calculating the effect that the surface has on the beads by using some assumptions on the nature of the forces. To do this, we start by considering the flow profile due to a point force in the presence of an infinite wall. This profile can be calculated directly as

$$\mathbf{v}_i = \mu_{ij}\mathbf{F}_j, \qquad \textbf{[S10]}$$

where μ_{ij} is Blake's mobility tensor (10). In the case of unbounded flow, Blake's tensor simplifies to the well known Oseen tensor:

$$\mu_{ij} = \frac{1}{8\pi\eta r}(\mathbf{I}_{ij} - \hat{\mathbf{r}}_{\mathbf{ij}}\hat{\mathbf{r}}_{\mathbf{ij}}), \qquad \textbf{[S11]}$$

where $\mathbf{r}_{ij}$ is the vector from a point force at j to another point i with magnitude r_{ij} and a direction given by the unit vector $\hat{\mathbf{r}}_{ij}$ and η is the viscosity of the solvent. Because of symmetry, one does not expect any motion in the bulk. However, in the presence of a wall, the additional terms in the mobility tensor, which actually correspond to image forces that enforce a zero velocity at the surface $v(z=0)=0$, create contributions that lead to a gradient in the self-mobilities and more. In what follows we will analytically show how one can obtain Eq. **1** in the text.

We will first consider a dumbbell rotor consisting of two beads each of radius a, at a height of h above the wall. To obtain rotational movement, we impose a force F on each of the beads perpendicular to the axis of the dumbbell and calculate the effect of the image force acting on it as a function of θ. The axis is then rotated through the angle θ, and the overall velocity can then be calculated by integration. For a sketch of this system, see Fig. S.2*a*. The velocity of the walker as a function of θ is given by

$$v_x(\theta) = \frac{F}{8\pi\eta}\left[\frac{3}{4}\cos\theta\left(\frac{1}{\lambda_-}-\frac{1}{\lambda_+}\right) - \frac{3}{2}\sin^2\theta\left(\frac{ah\lambda_-\lambda_+}{\Gamma^{5/2}}\right)\right], \qquad \textbf{[S12]}$$

where we introduce the functions $\lambda_- = h - a\cos\theta$, $\lambda_+ = h + a\cos\theta$, and $\Gamma = h^2 + a^2\sin^2\theta$. The average velocity is then the average of v_x over one cycle; i.e., $v_x = (1/2\pi)\int v_x(\theta)d\theta$. Before integrating, we can extract the height h from the denominator. Furthermore, if we assume that the height is proportional to the length of the chain (consistent with the experimental and simulation observations), we can write

$$v_x = \frac{F}{8\pi\eta h}f(\theta). \qquad \textbf{[S13]}$$

We now recall that $F = 6\pi\eta\nu a^2$ to obtain for a dumbbell walker $v_x \sim \nu a^2/h$. This form is similar to Eq. **1**. To include N beads, one can substitute $a \to Na$ to obtain

$$v_x = \frac{\nu N^2 a^2}{h}, \qquad \textbf{[S14]}$$

which is exactly Eq. **1**.

To corroborate that the last expression is the correct limiting behavior, we calculate the walking velocity of a chain consisting of N (even) beads. To describe the entire assembly we note that the chain is simply a sequence of dipole (two-bead) rotors that exists at increasing distance from the center of mass. We generalize Eq. **S14** to consider the effect of an image dipole of radius $d_k = a(2k+1)$ (where k is an integer index that describes the dipole rotor of interest) on a real dipole of radius $d_l = a(2l+1)$ (again, l is an integer index similar to k). We indicate this geometry in Fig. S2*b*. In determining the overall effect, we must sum over both k and l to account for all the dipole rotor to dipole rotor interactions. We also note that the force F now depends on k, because $F = 6\pi\nu\eta a d_k$, which is the drag force on the beads as a result of an applied frequency ν. To present a simplified general equation, we define the following functions:

$$\Delta_i = \begin{cases} d_k - d_l & i = \text{odd}, \\ d_k + d_l & i = \text{even}, \end{cases} \qquad \textbf{[S15]}$$

$$m_i = \begin{cases} +1 & i \le 2, \\ -1 & i > 2, \end{cases} \qquad \textbf{[S16]}$$

$$\alpha_i = 2h + m_i\Delta_{i+1}\cos\theta, \qquad \textbf{[S17]}$$

$$\beta_i = \alpha_i^2 + \Delta_i^2\sin^2\theta, \qquad \textbf{[S18]}$$

$$\lambda_i = h + m_i d_k\cos\theta, \qquad \textbf{[S19]}$$

$$\gamma_i = \begin{cases} (h + d_l\cos\theta)(h + d_k\cos\theta) & i = 1, \\ (h - d_l\cos\theta)(h + d_k\cos\theta) & i = 2, \\ (h - d_l\cos\theta)(h - d_k\cos\theta) & i = 3, \\ (h + d_l\cos\theta)(h - d_k\cos\theta) & i = 4. \end{cases} \qquad \textbf{[S20]}$$

The force along the x axis due to the hydrodynamic interactions on a dipole of arbitrary radius d_l due to another dipole with the same center of mass with arbitrary radius d_k is

$$f_{x,kl} \sim \eta\nu a^2 d_k\left[\cos\theta\sum_i^4\left(2m_i\gamma_i\left(\frac{3\Delta_i^2\sin^2\theta-\beta_i}{\beta_i^{5/2}} - \frac{\Delta_i^2\sin^2\theta+\beta_i}{\beta_i^{3/2}}\right)\right)\right.$$
$$\left. - \sin^2\theta\sum_i^4\Delta_i\left(\frac{\alpha_i - 2\lambda_i}{\beta_i^{3/2}} + \frac{6\gamma_i\alpha_i}{\beta_i^{5/2}}\right)\right]. \qquad \textbf{[S21]}$$

Finally, the total translational velocity of a rotor consisting of an arbitrary number of beads N is given by the summation of all the forces over all dipole rotors multiplied by the mobility of the assembly $(1/(\eta Na))$:

$$v_x \sim \frac{1}{\eta Na}\sum_{l=0}^{N/2}\sum_{k=0}^{N/2} f_{x,kl}, \qquad \textbf{[S22]}$$

where we sum to $N/2$ because each $v_{x,kl}$ corresponds to two beads of the chain.

The resulting v_x is a function of θ, and the analytical version given above can be compared to the velocity of the rotor center of

mass, which is shown in Fig. S3*a*. Excellent agreement between the two results is apparent, with minor differences likely as a result of the different mobility tensors used in the above analysis versus the simulations. For this comparison we have fitted the velocity at one point for the $N = 10$ beads to obtain the prefactor and used this throughout all the other calculations.

Finally, the average velocity of a long rotor can be obtained by performing the integration of v_x over a single rotation:

$$\langle v_x \rangle = \frac{1}{2\pi} \int_0^{2\pi} v_x d\theta. \quad \text{[S23]}$$

This integration was performed numerically, and the result is plotted in Fig. S2*b*. Notice that this result matches well with the simulation results despite all the approximations involved. We can directly verify that the velocity is proportional to N graphically, by plotting its behavior. The result is shown in Fig. S3*b*, which clearly shows that $v_x \sim N$, and thus $v_x \sim a\nu N$, further corroborating the validity of Eq. **1** in the text.

Scaling Relationship for Chain Fragmentation. The breakup (or fragmentation) of the paramagnetic chains is a result of the conflicting magnetic and frictional forces on the beads. We can describe the torque associated with both processes with simple scaling arguments. The torque input into the system due to the magnetic field is described by the relationship

$$\tau_B = m \times \mathbf{B} \sim mB. \quad \text{[S24]}$$

Because the value of the magnetic dipole m is linearly proportional to the number of beads N and the magnitude of the applied magnetic field B, the torque associated with the magnetic field is

$$\tau_B \sim NB^2. \quad \text{[S25]}$$

The frictional torque τ_F associated with a single bead i is given by the moment arm d_i, the velocity v_i, and the viscosity η. The relationship is

$$\tau_{F,i} \sim d_i v_i \eta \sim \nu d_i^2 \eta, \quad \text{[S26]}$$

where v_i is replaced by νd_i in the far right expression. This expression can be integrated over the length of the chain arm to yield the overall torque:

$$\tau_F \sim \int_0^N \nu d_i^2 \eta d(d_i) \sim \nu N^3 \eta. \quad \text{[S27]}$$

Fragmentation occurs when the frictional torque overcomes the magnetic torque. A characteristic frequency ν_c can be defined by the point at which τ_F/τ_B is on the order of unity:

$$\nu_c \sim \frac{B^2}{N^2 \eta}, \quad \text{[S28]}$$

which is the scaling relationship described in Eq. **2** in the main text.

Velocity Profile of a Single Rotor. We can calculate the simulated hydrodynamic field at a given point in space from the simulation by using the appropriate mobility tensors (9). In particular, we use a modified Blake's tensor μ_{ij} that accounts for the finite size of our beads (1, 2). The velocity field at point $\mathbf{r}_i$ due to a collection of beads j on which a force $\mathbf{F}_j$ acts is then given by (9)

$$\mathbf{v}(\mathbf{r}_i) = \sum_j^N \mu_{ij}(\mathbf{r}_i, \mathbf{r}_j)\mathbf{F}_j(\mathbf{r}_j). \quad \text{[S29]}$$

To calculate the contour plots in Fig. 4, we simply take the time average of the x component of this velocity at a given point over one period, $\langle \mathbf{v}_x \rangle_t$.

In order to check that our results are correct, we compare the velocity along the x direction as a function of the distance from the chain. In the far field, this system should decay proportional to $1/r_x^3$ (10). Fig. S4 shows the velocity profile along the x axis, which follows the expected decay.

Velocity Profile of an Ensemble of Rotors. As a first approximation, the velocity field produced by a set of rotors can be treated by the replacement of discrete rotors by an average area density of rotors ρ_S. If the system is sufficiently homogeneous, one can show that the overall velocity can be simply computed as

$$v(z) = \rho_S \beta(z). \quad \text{[S30]}$$

The function $\beta(z)$ corresponds to the integral of the single chain velocity field v_x along a given z plane, namely,

$$\beta(z) = \int v_x(x, y, z) dx dy. \quad \text{[S31]}$$

This approximation is typical of a classical mean-field velocity approximation. A simple way to see how this works out is to consider the rotors on a square lattice with lattice constant l. In this case the density is simply $\rho_S = 1/l^2$. If we approximate the velocity within one of the lattice squares by the average (mean) velocity in this square, we arrive at the formula given above. This result is thus valid if we can assume that the distribution of rotors is sufficiently homogeneous. Alternatively, we could take the approach of Kim and Netz (11), who derived the expression above for the area-averaged Blake mobility tensor (μ_{ij}) describing the effect of a spatially averaged force distribution on the average velocity at a given height z. This approximation effectively smears the spatial distribution of rotors (as we assumed before) such that the point forces on the rotors are homogeneously redistributed on a horizontal plane of fluid. The velocity is then given by

$$v_x(z_i) = \rho_S \int dz_j \mu_{ij}(z_i, z_j) F_x(z_j)/a, \quad \text{[S32]}$$

where $\rho_S F_x(z)/a$ is the laterally averaged force density applied at height z and μ_{ij} has the form

$$\mu_{ij}(z_i, z_j) = \begin{cases} z_j/\eta & z_i > z_j, \\ z_i/\eta & z_i < z_j. \end{cases} \quad \text{[S33]}$$

Both approaches yield the same result, though the former requires prohibitively large spatial averaging to yield the latter, which is the asymptotic limit. The latter function is evaluated directly from the simulations and is plotted in Fig. 4 for a walker consisting of seven beads. The value of β is also a function of the number of beads in the chain [Fig. S4 plots the maximum value of $\beta(z)$, i.e., $\beta_{\max}$, as a function of N] and demonstrates a large increase with chain length.

The approach of Kim and Netz (11) also allows for the derivation of an analytical form of β as a function of the basic parameters in this system. We specifically consider only the case where $h = Na$, which is the geometry present in our experiments and simulations. In this system, if we consider a nonbending rod of length $2h$ as an approximation of the discrete chain, the force density $F(z)/a$ at a given height from the surface z is independent of the angle of the rotor as it rotates and is given by the equation

$$F(z)/a = 6\pi\eta\nu(z - h). \quad \text{[S34]}$$

Whereas the force density is independent of the angle of the rotor, the angle of the rotor determines whether or not there

is a force applied to the fluid by the rotor at a given height z. For example, if the rotor is fully orthogonal to the surface, the rotor imparts a force at every z between $z = 0$ and $z = 2h$; however, it feels this force only for an infinitely small time. As soon as the angle of rotation changes, the rod no longer imparts a force corresponding to the $z = 0$ and $z = 2h$ extremes. In contrast, the heights close to the center of the rotor at $z = h$ almost always feel a force (though not directly at $z = h$, because there is no rotational force there). We can thus multiply $F(z)/a$ by a fraction $f(z)$ that represents the portion of time during rotation that a force is being applied to a given height z with respect to the surface. The final form of $f(z)$ is

$$f(z) = \begin{cases} 0 & z > 2h, \\ \frac{2}{\pi}\arccos(\frac{z-h}{h}) & 2h > z > h, \\ \frac{2}{\pi}\arccos(\frac{h-z}{h}) & h > z > 0. \end{cases} \quad \textbf{[S35]}$$

Unfortunately, the arccosine function is inconvenient to integrate and ultimately yields a very complicated result for $\beta(z)$. To simplify both the integration and the final form of $\beta(z)$, we approximate $f(z)$ as

$$f(z) = \begin{cases} (\frac{2h-z}{h}) & 2h > z > h, \\ (\frac{z}{h}) & h > z > 0. \end{cases} \quad \textbf{[S36]}$$

We note that this approximation underestimates the amount of force that the rotor imparts upon the surrounding fluid by a small amount; however, it still retains the limits of 0 at $z = 0$, $2h$, and 1 at $z = h$. These functions can then be integrated with the averaged mobility tensor $\mu_{ij}(z_i, z_j)$ to obtain $\beta(z)$:

$$\beta(z) = \int_0^\infty dz_j \mu_{ij}(z, z_j) F_x(z_j) f(z_j)/a. \quad \textbf{[S37]}$$

The evaluation of this integral results in Eq. **6** of the main paper:

$$\beta(z) = \begin{cases} \pi\nu z^3(1 - \frac{z}{2h}) & z < h, \\ \pi\nu(h^3 - 4h^2 z + 6hz^2 - 3z^3 + \frac{z^4}{2h}) & h < z < 2h, \\ \pi\nu h^3 & z > 2h. \end{cases} \quad \textbf{[S38]}$$

To highlight the similarity of the form of this analytical result to the profile obtained from the simulation data, we plotted the normalized $\beta(z)/\beta_{\max}$ in Fig. 4*A*. The values of the analytical and simulation results for $\beta_{\max}$ are compared in Fig. S5, which shows that these values are of the same order of magnitude and increase with a similar trend. The analytical solution is lower in value than the simulations; however, this result is expected because of the significant approximations made in the derivation of the above equation [the flexible bead chain is replaced by a rigid rod, and the form of $f(z)$ is simplified]. Finally, these results are used to estimate the order of magnitude expected for the corresponding experimental realization and seem to agree well with the experiments.

1. Blake JR (1971) A note on the image system for a stokeslet in a no-slip boundary. *P Camb Philos Soc* 70:303.
2. Jones RB, Kutteh R (1999) Sedimentation of colloidal particles near a wall: Stokesian dynamics simulations. *Phys Chem Chem Phys* 1:2131–2139.
3. Kim YW, Netz RR (2006) Electro-osmosis at inhomogeneous charged surfaces: Hydrodynamic versus electric friction. *J Chem Phys* 124:114709.
4. Kim YW, Netz RR (2006) Pumping fluids with periodically beating grafted elastic filaments. *Phys Rev Lett* 96:158101.
5. Alexander-Katz A, Netz RR (2007) Surface-enhance unfolding of collapsed polymers in shear flow. *Europhys Lett* 80:18001.
6. Pankhurst QA, Connolly J, Jones SK, Dobson J (2003) Applications of magnetic nanoparticles in biomedicine. *J Phys D Appl Phys* 36:R167–R181.
7. Gijs MAM (2004) Magnetic bead handling on-chip: New opportunities for analytical applications. *Microfluid Nanofluid* 1:22–40.
8. Angelova MI, Dimitrov DS (1986) Liposome electroformation. *Faraday Discuss* 81:303–311.
9. Kim S, Karrila SJ (1991) *Hydrodynamics: Principles and Selected Applications* (Butterworth–Heinemann, Boston).
10. Blake JR, Chwang AT (1974) Fundamental singularities of viscous flows. *J Eng Math* 8:23–29.
11. Kim YW, Netz RR (2006) Electro-osmosis at inhomogeneous charged surfaces: Hydrodynamic versus electric friction. *J Chem Phys* 124:114709.

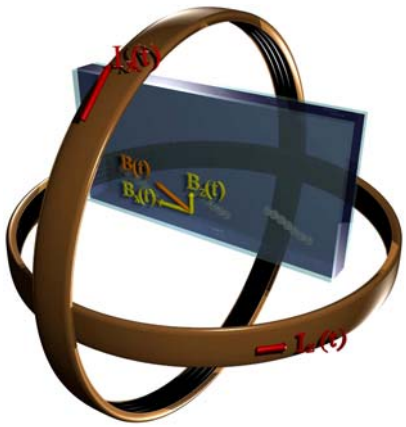

Fig. S1. A figure demonstrating the experimental setup used to probe the behavior of superparamagnetic colloids. Phase-shifted sinusoidal currents I_x and I_z impart a rotating magnetic field at the center of the coils. Not shown is a viewing window through the coils where they intersect to allow for sideways viewing of the rotors.

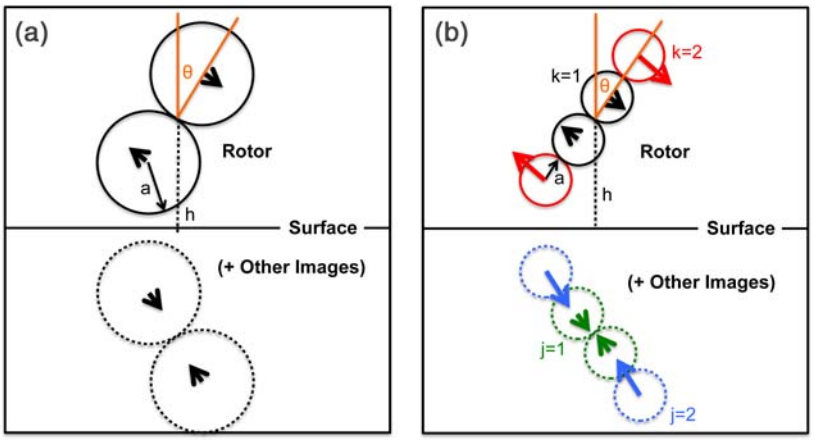

Fig. S2. (*a*) Schematic describing the geometry of a hydrodynamic dipole ($N = 2$). The no-slip boundary condition at the surface is imposed upon the addition of the image chain (dashed beads) plus other images (not shown in this diagram), whose hydrodynamic effect on the real rotor is what drives the translational motion. The geometry of this chain is characterized by the bead radius *a*, the height of the rotor *h*, and the angle of the dipole from the vertical axis θ. The equations relating to this geometry can be generalized to describe the behavior of chains with $N > 2$, such as in (*b*). Here, there are two dipoles with different distances from the center of the rotor ($k = 1, 2$) with two image chains ($j = 1, 2$) (other images not shown). The interactions of the image dipoles with the real dipoles becomes more complicated, as each image affects each real dipole.

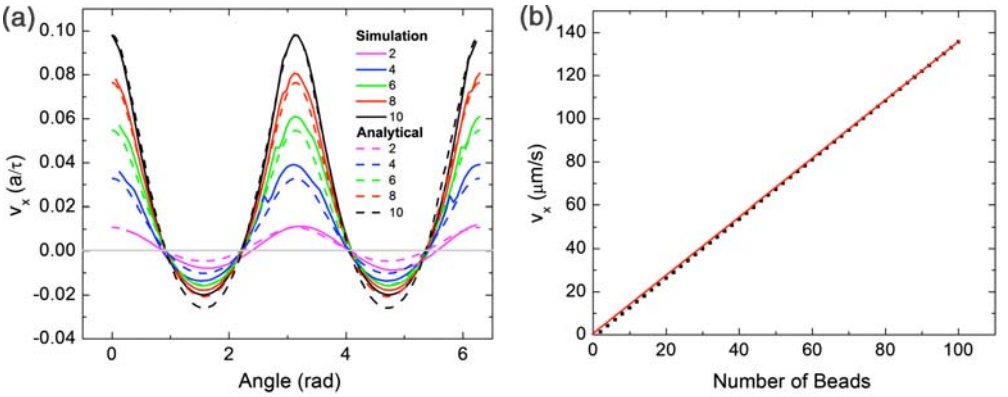

Fig. S3. (*a*) The analytical and simulation results describing the angular dependence on the rotor's translational velocity v_x as a function of the number of beads in the chain *N*. Notice that both results are in good agreement. (*b*) Upon integration of curves such as those in (*a*), we can obtain the analytical result for the translational velocity of a rotor with an arbitrary number of beads. Results for 2–100 beads are plotted to demonstrate that the linear relationship between v_x and the number of beads is realized for large rotors. The black points are the analytical results, and the red line is a straight line meant to guide the eye and demonstrates the agreement with a linear relationship.

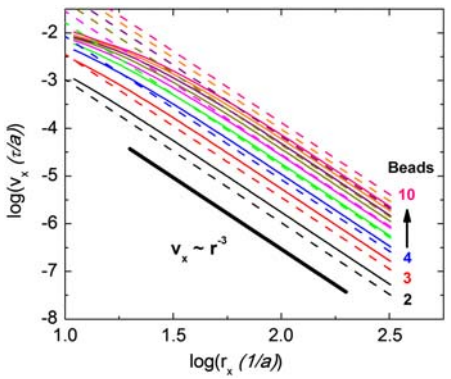

Fig. S4. The plot of the flow profile of multibead rotors at a frequency of 18.5 Hz taken from simulation data. The *y* axis is the natural log of the velocity in the *x* direction, and the *x* axis is the natural log of the radial distance along the *x* axis. The dotted lines are taken from ref. 10 using parameters in the simulation for various rotor lengths.

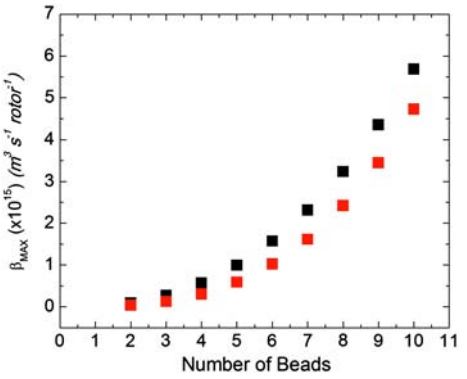

Fig. S5. The plot of β_{max} for $\nu = 1.5$ Hz as a function of chain length as measured from simulation data (black) and calculated from the analytical function given in Eq. **6** of the paper (red).

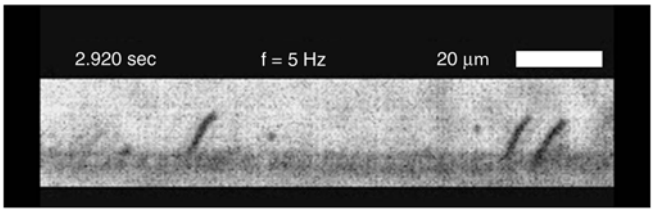

Movie S1. Lateral view of colloidal self-assembled chains rotating on a surface. The frequency is varied to show the fragmentation transition. Notice how the chains are translating along the surface.
Movie S1 (MPG)

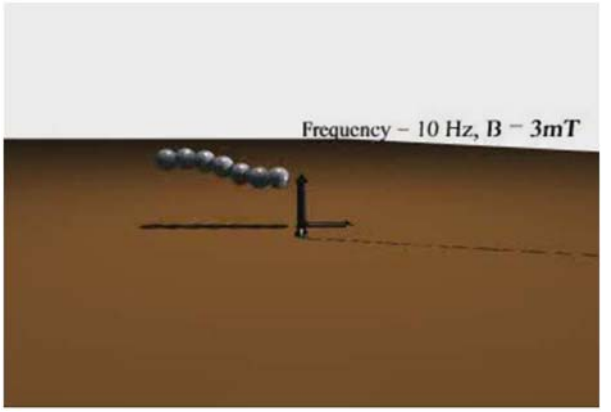

Movie S2. Computer simulation of a colloidal self-assembled chain rotating on a surface. The frequency is varied to show the fragmentation transition. Notice how the chain is translating along the surface. Also notice the agreement with the experimental results in Movie S1.
Movie S2 (MPG)

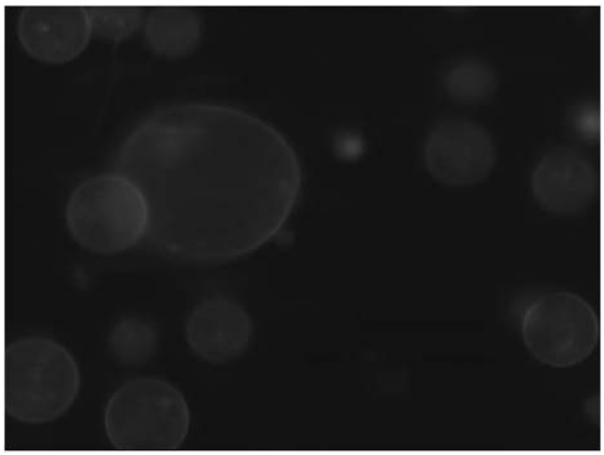

Movie S3. Movie of fluorescently labeled vesicles dancing to a Bavarian Waltz. The vesicles are being moved by a collection of surface walkers that are rotating on the surface with the direction of rotation determining the direction of motion. The colloidal chains (or surface walkers) are shown in the second part of the movie when the microscope is changed from fluorescent to bright field mode.

Movie S3 (MPG)